Check for updates

RESEARCH ARTICLE

NANO · MICRO small
www.small-journal.com

Nanoribbon Yarn with Versatile Inorganic Materials

Junseong Ahn, Yongrok Jeong, Mingu Kang, Jihyeon Ahn, Suchithra Padmajan Sasikala, Inyeong Yang, Ji-Hwan Ha, Soon Hyoung Hwang, Sohee Jeon, Jimin Gu, Jungrak Choi, Byung-Ho Kang, Sang Ouk Kim, Sanha Kim, Junhyuk Choi, Jun-Ho Jeong, and Inkyu Park**

Nanomaterial-based yarns have been actively developed owing to their advantageous features, namely, high surface-area-to-volume ratios, flexibility, and unusual material characteristics such as anisotropy in electrical/thermal conductivity. The superior properties of the nanomaterials can be directly imparted and scaled-up to macro-sized structures. However, most nanomaterial-based yarns have thus far, been fabricated with only organic materials such as polymers, graphene, and carbon nanotubes. This paper presents a novel fabrication method for fully inorganic nanoribbon yarn, expanding its applicability by bundling highly aligned and suspended nanoribbons made from various inorganic materials (e.g., Au, Pd, Ni, Al, Pt, WO_3, SnO_2, NiO, In_2O_3, and CuO). The process involves depositing the target inorganic material on a nanoline mold, followed by suspension through plasma etching of the nanoline mold, and twisting using a custom-built yarning machine. Nanoribbon yarn structures of various functional inorganic materials are utilized for chemical sensors (Pd-based H_2 and metal oxides (MOx)-based green gas sensors) and green energy transducers (water splitting electrodes/triboelectric nanogenerators). This method is expected to provide a comprehensive fabrication strategy for versatile inorganic nanomaterials-based yarns.

1. Introduction

Recently, nanomaterial-based yarn structures have been widely utilized owing to their unique features: the superior properties of the nanomaterial can be directly imparted and scaled-up to macro-sized structures. Representatively, fully suspending the structures of nanomaterials can maximize the surface-area-to-volume (SA:V) ratio.[1,2] In addition, the mechanical flexibility of nanomaterials can be imparted to macro-sized structures, which is advantageous in flexible device applications of hard and brittle materials.[3] Lastly, unusual material characteristics such as anisotropy in electrical/thermal properties can be obtained on the macro-scale because of the directionality of the yarn structure.[2,4] The unique features of the nanomaterial-based yarn enable original applications such as flexible gas sensors based on graphene nanoribbon yarn[5] and high efficiency thermoelectric generators using n/p-doped carbon nanotube yarn.[6,7] Furthermore, this structure can replace the thread, the unit of the fabric, and can thus be easily utilized in various wearable applications such as the wearable triboelectric nanogenerator (TENG)[8–10] and wearable fiber supercapacitor.[10–12]

Despite the superior properties of the previously developed nanomaterial-based yarns and their promise in respective applications, there are challenges associated with specialized usage due to the lack of material versatility. For example, CNT-based yarn has been utilized in gas sensing applications, and much effort has been expended to improve its performance.[13] However, there is an intrinsic limitation such as low sensitivity that can be resolved by replacing the material, especially with specific and functionalized inorganic materials. Although comprehensive fabrication methods (fabrication of CNT/graphene-based yarn by physical vapor deposition (PVD)[14–17] and fabrication of polymer yarn by highly aligned electrospinning[18,19]) have already been developed for organic nanomaterial-based yarns, there are no common methods for the fabrication of inorganic nanomaterial-based yarns. To form the inorganic material into a nanomaterial yarn shape, previous studies have suggested hybrid methods of organic/inorganic materials and very few methods have been suggested for fully-inorganic

J. Ahn
Department of Electro-Mechanical Systems Engineering
Korea University
Sejong 30019, Republic of Korea
Y. Jeong
Radioisotope Research Division
Korea Atomic Energy Research Institute
111, Daedeok-daero, Yuseong-gu, Daejeon 34 057, Republic of Korea
M. Kang, J. Ahn, I. Yang, J.-H. Ha, J. Gu, J. Choi, B.-H. Kang, S. Kim, I. Park
Department of Mechanical Engineering
Korea Advanced Institute of Science and Technology
291, Daehak-ro, Yuseong-gu, Daejeon 34 141, Republic of Korea
E-mail: inkyu@kaist.ac.kr
S. Padmajan Sasikala, S. O. Kim
Department of Materials Science & Engineering
Korea Advanced Institute of Science and Technology
291, Daehak-ro, Yuseong-gu, Daejeon 34 141, Republic of Korea
S. H. Hwang, S. Jeon, J. Choi, J.-H. Jeong
Department of Nano-manufacturing Technology
Korea Institute of Machinery and Materials
156, Gajeongbuk-ro, Yuseong-gu, Daejeon 34103, Republic of Korea
E-mail: jhjeong@kimm.re.kr
The ORCID identification number(s) for the author(s) of this article can be found under https://doi.org/10.1002/smll.202311736

DOI: 10.1002/smll.202311736

 © 2024 Wiley-VCH GmbH

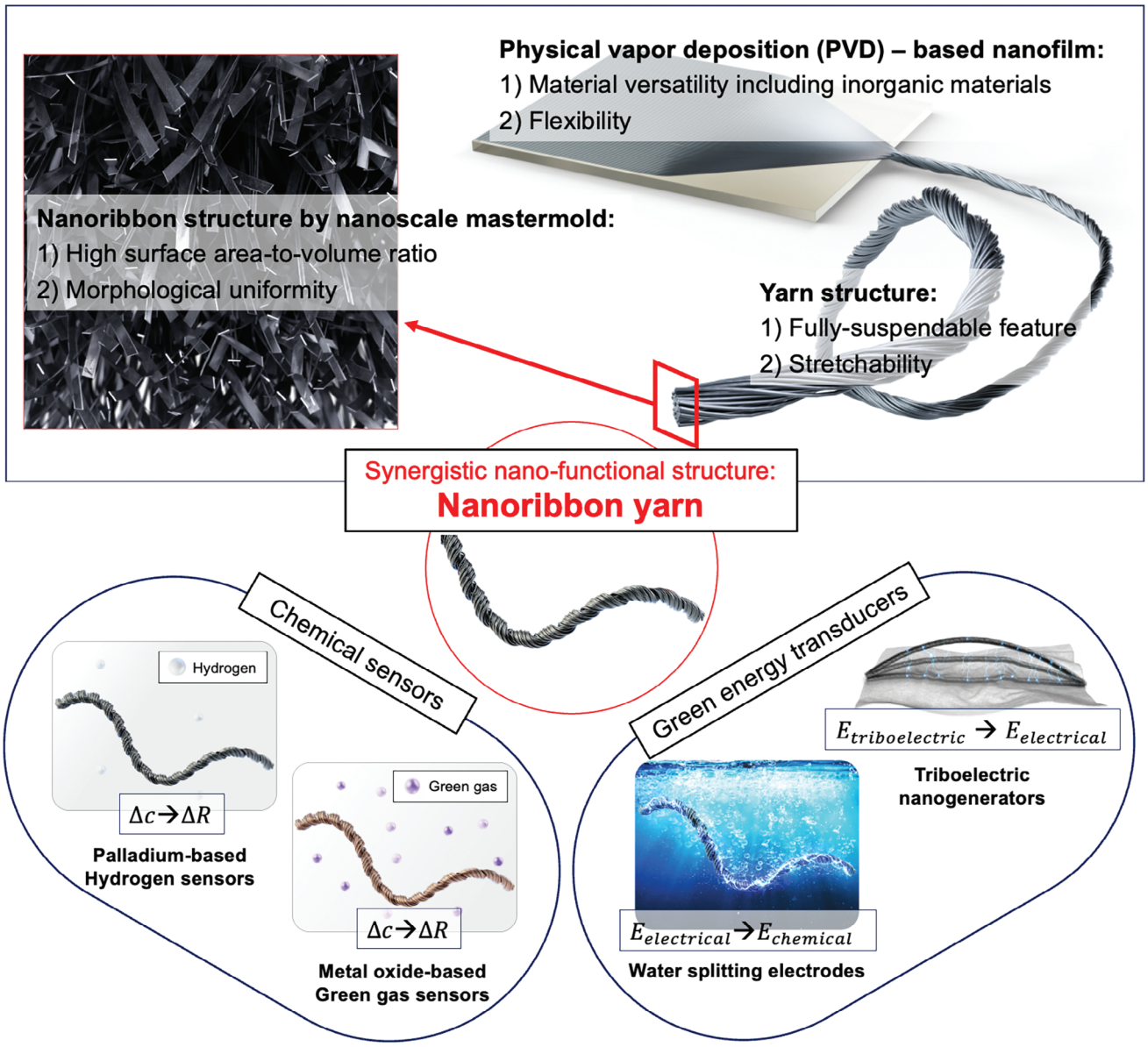


Figure 1. Overview of the characteristics of the nanoribbon yarn: The characteristics of the proposed nanoribbon yarn originate from three features: PVD-based fabrication and the yarn and nanoribbon structures. These characteristics enable the unique features of the nanoribbon yarn: high surface-area-to-volume (SA:V) ratio and stretchability. Owing to these features, nanoribbon yarn may be used as chemical sensors (Pd-based H_2 and metal oxides (MOx)-based green gas sensors), and green energy transducers (water splitting electrodes, triboelectric nanogenerators).

nanomaterial-based yarns (Table S1, Supporting Information). However, hybrid methods cannot fabricate the fully-inorganic yarns, which limits the effective utilization of inorganic materials. Previous research to fabricate fully-inorganic nanomaterial-based yarns include fabrication using calcination of the aligned polymer nanoyarn[20] and fluid-spinning of the metal oxide,[21] but these methods still do not suffice to cover the broad scope of inorganic materials. If the material scope of the nanomaterial-based yarn can be broadened to general inorganic materials, then the abovementioned applications can meet the technical breakthrough. For example, semiconducting gas sensors frequently utilize metals (Pd for sensing H_2) or metal oxides (SnO_2 for reactive gas sensing) instead of carbon-based materials owing to their superior sensitivity. The fabrication of metal or metal oxide nanomaterial-based yarn can notably enhance the sensitivity of flexible gas sensors.

This paper presents a simple method to fabricate nanoribbon-based yarn with versatile materials (**Figure 1**). The proposed inorganic nanoribbon yarn possesses unique properties originating from the PVD–based nanofilm, yarn structure, and nanoribbon structure. The PVD-based nanofilm enables material versatility, including inorganic materials, and the nanoscale thickness of the film realizes the flexibility for overall structure. The yarn exhibits a fully suspendable and stretchable morphology

© 2024 Wiley-VCH GmbH

16136829, 2024, 38, Downloaded from https://onlinelibrary.wiley.com/doi/10.1002/smll.202311736 by Korea University Library, Wiley Online Library on [19/09/2024]. See the Terms and Conditions (https://onlinelibrary.wiley.com/terms-and-conditions) on Wiley Online Library for rules of use; OA articles are governed by the applicable Creative Commons License

without any additional substrates or treatments, even for brittle materials such as MOx. The nanoribbon structure imparts an intrinsic high SA:V, which is advantageous for energy-related applications.[8,12,16,22,23] Based on these morphological advantages, the synergistic nano-functional structure, namely nanoribbon yarn, is fabricated. The fabricated nanoribbon yarn exhibits superior in-sample and sample-to-sample uniformity, as demonstrated by the electrical resistance uniformity (107.4 Ω m^{-1} on average, 0.83% of relative standard deviation (RSD) and 112.4 Ω m^{-1} on average with RSD of 4.2%, respectively). Finally, it is utilized in high-performance chemical sensing (e.g., Pd-based H_2 and metal oxides (MOx)-based green gas sensors) and green energy transducing applications (e.g., water splitting electrodes and triboelectric nanogenerators).

2. Results and Discussion

2.1. Fabrication of Nanoribbon Yarn

The research starts with the fabrication and characterization of nanoribbon yarn structure. Versatile materials were deposited onto a nanoimprinted polyurethane acrylate (PUA) mold by electron beam (E-beam) deposition (**Figures** 2a-i; S1a, Supporting Information). The PUA mold was undercut using a plasma-assisted etching method (reactive ion etching (RIE)), and suspended structures of the nanoribbons formed as a result (Figures 2a-ii, iii; S1b and Figure S2, Supporting Information). Afterwards, the nanoribbons were delaminated from the substrate and twisted to form a nanoribbon yarn (Figure 2a-iv; Figure S1c, Supporting Information). The nanoribbon yarn was twisted using two different methods in this research: hand-twisting (Figure S1c-iii, Supporting Information) and machine-twisting (Figure S1c-iv, Supporting Information). Details of the fabrication process can be found in the Methods section. The fabricated nanoribbon yarn (hand-twisting) is shown in Figure 2b–d. Nanoribbon yarn was successfully fabricated (Figure 2b-i) and analyzed via scanning electron microscopy (SEM) (Figure 2b-ii, iii); the analysis revealed a yarn structure with a uniformly aligned nanoribbon. Additionally, the cross-sectional images of the nanoribbon yarn (Figure 2c-i) confirm that the nanoribbon structure was maintained during twisting. Further, because the nanoribbons stand individually without any binding, the SA:V could be effectively maximized (Figure 2c-ii; Note S1, Supporting Information). The composition of the nanoribbon yarn was confirmed by observing the energy-dispersive X-ray spectroscopy (EDS) image of this cross section (Figure S3, Supporting Information). Although the nanoribbon yarn shown in Figure 2 shows only the morphology of a line pattern (pitch of 2000 nm and width/space of 1200 nm/800 nm) with a PVD thickness of 100 nm, nanoribbon yarns with different morphologies were also fabricated. From the nanoline mold with a smaller scale (pitch: 2000 nm → 400 nm, width: 800 nm → 200 nm) and smaller PVD thickness (100 nm → 30 nm) of the target material, the successful fabrication of nanoribbon yarn was also confirmed (Figure S4, Supporting Information).

Materials that satisfy the following two conditions can be fabricated with a nanoribbon yarn morphology: the material can be deposited by PVD and affected minutely by plasma-assisted etching. Various materials can be deposited via E-beam deposition. A few representative metals and metal oxides were selected and successfully fabricated with a nanoribbon yarn morphology. In this research, nanoribbon yarn comprising metals, such as Au, Pd, Ni, Al, and Pt (Figure 2d), and metal oxides, such as tungsten oxide (WO_3), tin oxide (SnO_2), nickel oxide (NiO), indium oxide (In_2O_3), and copper oxide (CuO) (Figure 2e) were fabricated. The EDS data confirmed that the deposited metals and metal oxides were successfully fabricated in the morphology of nanoribbon yarn with the desired types of materials.

2.2. Uniformity of Nanoribbon Yarn

Intrinsically, the hand-twisting process displays low uniformity, due to human error. A machine-twisting process was developed to replace the hand-twisted process with a custom-built twisting machine (Figure S1c-iv and S5a, Supporting Information) to increase the uniformity. In this experiment, the previous nanopatterned mold (pitch of 2000 nm and width/space of 1200 nm/800 nm) was also replaced by the new nanopatterned mold (pitch of 1600 nm and width/space of 800 nm/800 nm) specifically designed for producing a nanoribbon yarn composed solely of nanoribbons with an 800 nm linewidth to enhance the uniformity of the yarn (Figure S5b, Supporting Information). The first validation performed on the standardized yarn produced by this process was a within-sample uniformity test, which was performed with sample of lengths greater than 10 cm (**Figure** 3a). Three characteristics (resistance per unit length, diameter, and twist angle) were measured: The resistance per unit length provides an indication of the overall uniformity of the yarn, and the diameter and twist angle provide an indirect indication of the twisting mechanism. The resistance per unit length showed a uniform value regardless of the location (107.4 Ω m^{-1} on average, 0.83% of relative standard deviation ((RSD), Figure 3b), indicating that the yarn is well organized with a uniform number of nanoribbons. Next, the twist morphology indicates that the middle section has a smaller diameter (187 μm) and a steeper twist angle (≈24°) compared with that of the average, while the two ends have a larger diameter (220 μm) and a gentler twist angle (≈19°) (Figure 3c). Because the twist angle is directly related to the number of turns per unit length, it can be interpreted that the central part has a relatively higher number of turns per unit length than that of the outer part. The reason for this geometry can be found in the twisting process. The twisting process densifies the nanoribbon, reducing the diameter and increasing the twist angle. Because the boundaries (contact points of yarns with carbon tapes: both ends of the nanoribbon yarn) should be fixed during the initial state, it is expected that further twisting tendency will be concentrated in the center, resulting in a minimized diameter and a maximized twisting angle in the center of the yarn.

The second validation performed was a between-sample uniformity test (Figure 3d), which was performed on five newly fabricated samples and displayed an average value of 112.4 Ω m^{-1} (Figure 3e, RSD = 4.2%), 184.2 μm diameter (Figure 3f, RSD = 14.1%), and 20.7° twist angle (Figure 3f, RSD = 7.8%), confirming that the samples can be repeatedly fabricated within 15% RSD. This series of inspections confirms that the

© 2024 Wiley-VCH GmbH

16136829, 2024, 38, Downloaded from https://onlinelibrary.wiley.com/doi/10.1002/smll.202311736 by Korea University Library, Wiley Online Library on [19/09/2024]. See the Terms and Conditions (https://onlinelibrary.wiley.com/terms-and-conditions) on Wiley Online Library for rules of use; OA articles are governed by the applicable Creative Commons License

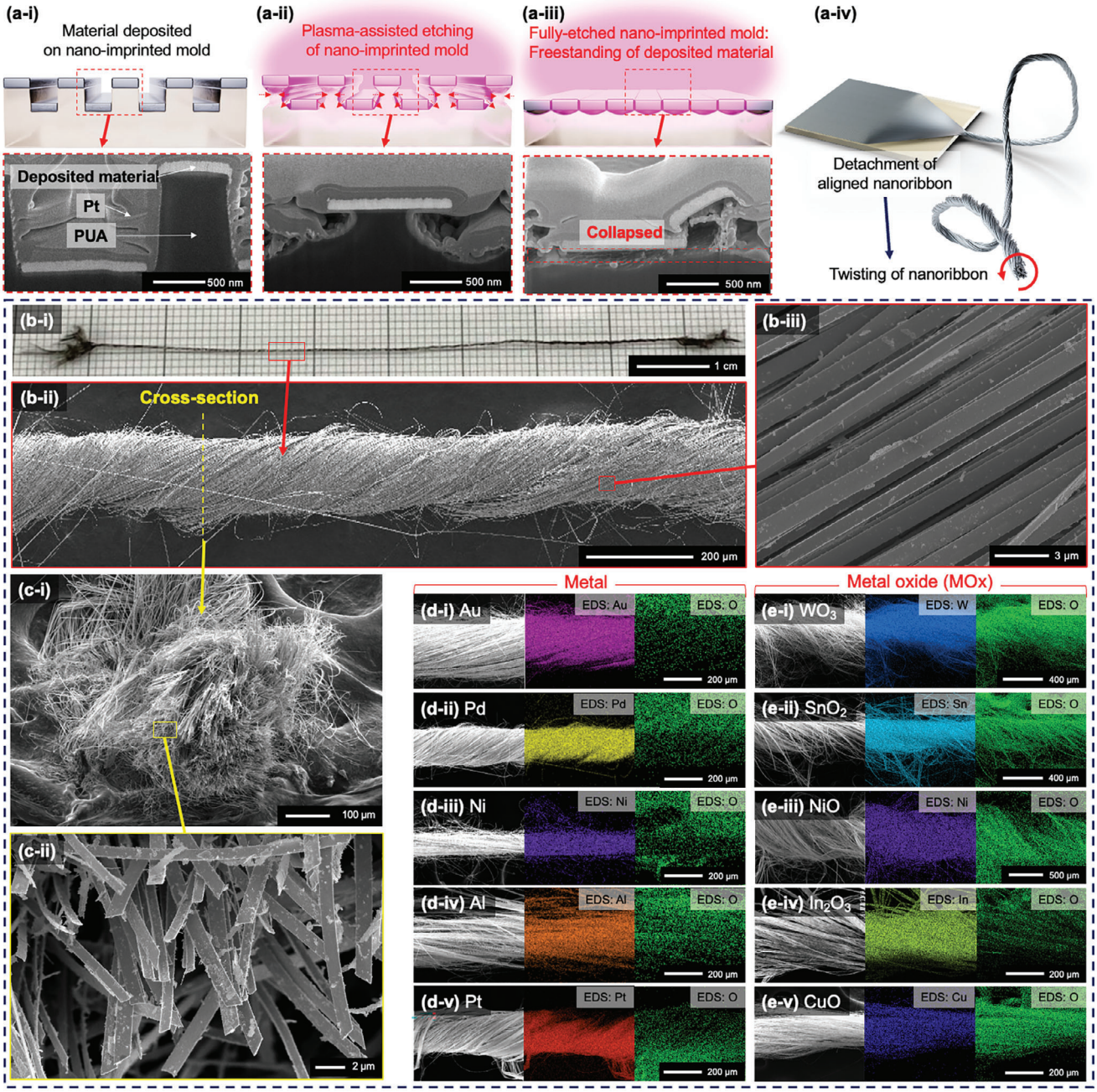


Figure 2. Fabrication of nanoribbon yarn using versatile materials: a-i) Versatile-material-deposited nanoimprinted mold. a-ii, a-iii) Plasma-assisted etching. a-iv) Detachment and twisting of nanoribbon yarn; b-i) Top view of the fabricated nanoribbon yarn (Pd), as observed by a naked eye. b-ii, b-iii) Top view of the fabricated nanoribbon yarn (Pd) observed by SEM; e) Cross-sectional view of the fabricated nanoribbon yarn (Pd) observed by SEM; d) Nanoribbon yarn fabricated with various metals (Au, Pd, Ni, Al, and Pt); (e) Nanoribbon yarn fabricated with various metal oxides (WO_3, SnO_2, NiO, In_2O_3, and CuO).

machine-twisting process displays reasonable within-sample and between-sample uniformity.

2.3. Mechanical Characterization of Nanoribbon Yarn

In general, the physical characterization of yarns typically requires stress-strain tests. However, obtaining a stress-strain curve of a nanoribbon yarn is challenging because of the low load-bearing capacity of nanoribbons. Therefore, we opted for an indirect approach measuring the electrical resistance changes with strain to glean insight into nanoribbon behavior.

Our study involved four different types of samples, encompassing ductile (Au) and brittle materials (In_2O_3). Each material was examined in two different morphologies: nanoribbon array and nanoribbon yarn. The primary observation was the

© 2024 Wiley-VCH GmbH

16136829, 2024, 38, Downloaded from https://onlinelibrary.wiley.com/doi/10.1002/smll.202311736 by Korea University Library, Wiley Online Library on [19/09/2024]. See the Terms and Conditions (https://onlinelibrary.wiley.com/terms-and-conditions) on Wiley Online Library for rules of use; OA articles are governed by the applicable Creative Commons License

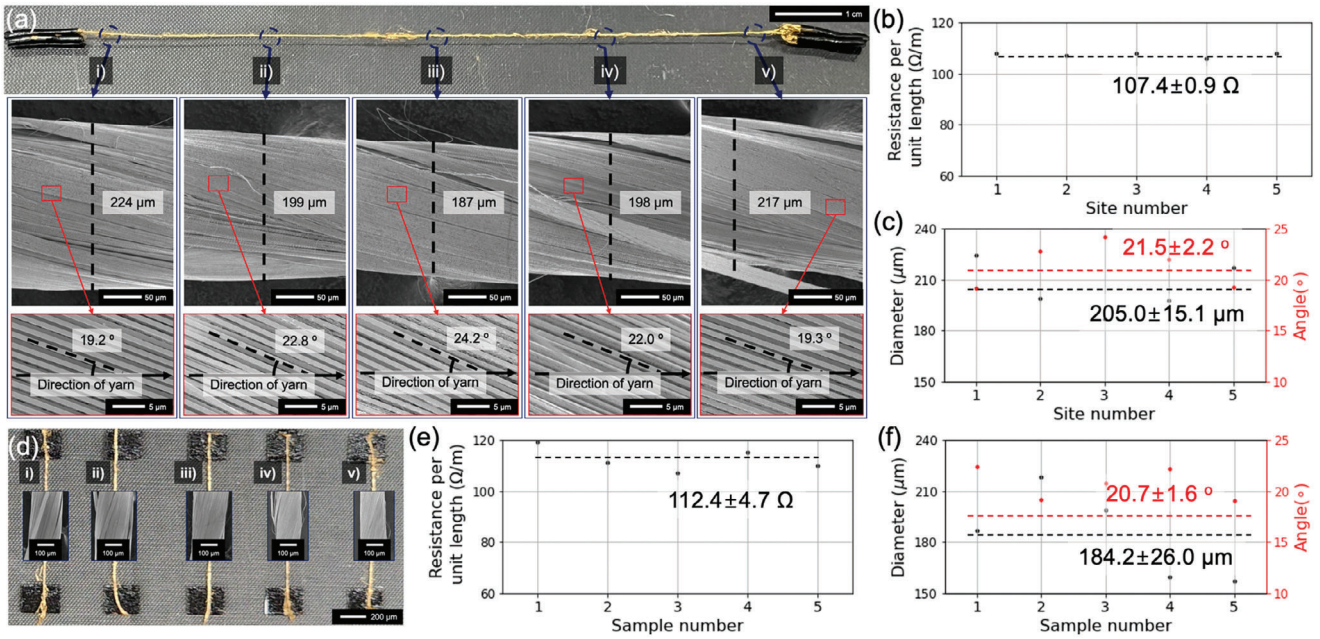


Figure 3. Uniformity test result for the machine-twisted nanoribbon yarn: The uniformity test was performed with the Au nanoribbon yarn. a–c) Within-sample uniformity test result. (a) Detailed images of the (i) leftmost, (ii) left, (iii) center, (iv) right, and (v) rightmost section of the fabricated long nanoribbon yarn (length of ca. 10.3 cm). (b) Resistance per unit length, and (c) Inspected diameters and twist angles for different sections; d–f) Between-sample uniformity test result. (d) Overview and (inset) detail images of the five different nanoribbon yarns (i-v). e) Resistance per unit length, and f) Inspected diameters and twist angles for each nanoribbon yarns.

exceptional electrical stability exhibited by nanoribbon yarns under tensile strain, usually less than 10%. Specifically, at a 10% strain, Au nanoribbon yarn displayed a change in resistance ($\Delta R/R_0$) of 0.048, while Au suspended nanoribbon arrays showed a $\Delta R/R_0$ of 4.17. For In_2O_3, the nanoribbon yarn exhibited a $\Delta R/R_0$ of −0.084, whereas In_2O_3 suspended nanowires displayed a $\Delta R/R_0$ of 12.6 (**Figure** 4a–d). Given that the fundamental morphology of the constituents for each sample remains identical and consists of nanoribbons, this phenomenon is believed to be induced by the unique twisted yarn structures. Before forming the nanoribbon yarn, a compressive pre-strain of 10% was applied to suspend the nanoribbon array, creating a sagging state. During the twisting process to form the yarn, the initially sagged nanoribbon array becomes twisted into a yarn structure and tightened as straight shape. As a result, the final length of the nanoribbon yarn is 10% shorter than the initial length of the nanoribbon array. Consequently, when strain is applied to the yarn, it mildly unravels and absorbs the strain without any significant electrical resistance change, even for the brittle metal oxide-based yarn.

Similarly, bending tests for Au and In_2O_3 nanoribbon yarns were also performed. These tests revealed resistance changes of 0.11% and −0.04% at a curvature of 1.3 cm^{-1}, respectively (Figure 4e). Further 1000 cyclic tests with strain and bending for Au nanoribbon yarn confirmed the ability of the structure of the yarn to maintain stable electrical contact within the nanoribbon network when subjected to external mechanical stimuli. Throughout 1000 cycles of repeated stretching and bending, the nanoribbon yarn consistently delivered a stable electrical resistance with alterations of less than 0.61% and 0.72%, respectively (Figure 4f,g). Consequently, the proposed nanoribbon yarn exhibits the potential to replace conventional single-body electrical wires, enabling stable operations in stretchable and flexible electronic interconnections and devices.

2.4. Green Energy Applications of Nanoribbon Yarn: Chemical Sensors and Energy Transducers

2.4.1. Chemical Sensors: Metal and MOx-Based Gas Sensors

Owing to its eco-friendliness, which is directly connected with sustainability, green energy is among the most important directions in the development of energy technologies. Currently, nanoscale functional materials are used in green technologies owing to the high SA:V that can maximize the efficiency of energy-related reactions.[24] Previous researchers used high-SA:V nanostructures such as silver nanowires and graphene to fabricate practical nanoscale functional materials.[14,15,25,26] Typically, two methods have been adopted for the use of prefabricated nanostructures: spreading onto the prepared substrate[25,26] or directly growing from the substrate.[14,15] However, both methods involve using substrates, and adverse effects such as reduced SA:V and reliability arise from substrate–nanomaterial interfaces.[1,2] To eliminate such issues, suspending nanomaterials has been attempted. However, the suspended nanomaterials, which are represented with the nanomaterial-based yarn, have been restricted in organic materials, as mentioned above.

Among various green energy technologies, green chemical energy, especially H_2, has attracted attention owing to its cost-effectiveness for decarbonization, high energy storing density, applicability in various energy systems, and facile energy transmission.[27] In usage, because H_2 is highly inflammable,

© 2024 Wiley-VCH GmbH

16136829, 2024, 38, Downloaded from https://onlinelibrary.wiley.com/doi/10.1002/smll.202311736 by Korea University Library, Wiley Online Library on [19/09/2024]. See the Terms and Conditions (https://onlinelibrary.wiley.com/terms-and-conditions) on Wiley Online Library for rules of use; OA articles are governed by the applicable Creative Commons License

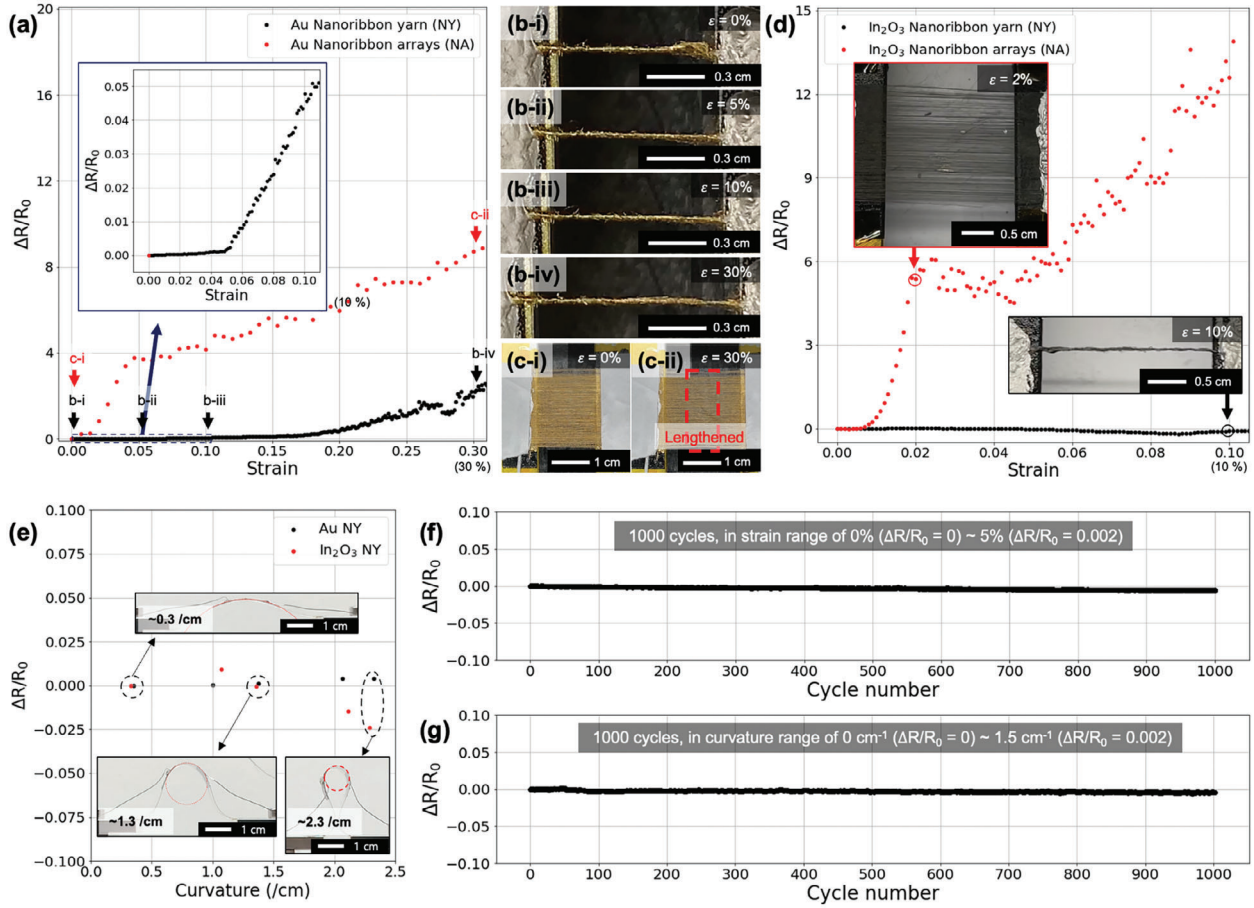


Figure 4. Results of the strain and bend test to confirm the stretchability and bendability of nanoribbon yarn: a–d) Relationship between normalized resistance ($\Delta R/R_0$) and strain (ε) for nanoribbon yarn and the untwisted nanopattern, with two representative materials of ductile (Au) and brittle (In_2O_3) materials. Within small strain change ($\varepsilon \approx 0.1$), the nanoribbon yarn shows stable resistance ($\Delta R/R_0 = 0.048$, -0.084 for Au and In_2O_3, respectively). The strain test result of Au nanoribbon yarn (NY) and nanoribbon array (NA) can be found in (a), and that for In_2O_3 NY and NA can be found in (d). Corresponding test images can be found in (b-c) and inset of (d); e) Result of the bend test for Au and In_2O_3 NYs. The bend test confirms that both nanoribbon yarns display stable resistance with at least $\approx$1.3 cm^{-1} of curvature. (Inset) Example images for various experimental conditions; f) Cyclic test result for a strain of 5% for 1000 cycles. Maximum 0.61% change in normalized resistance was observed; g) Cyclic test result for a curvature of 1.5 cm^{-1} for 1000 cycles. Maximum 0.72% of change in normalized resistance was observed.

quick monitoring of unintentional leaks is particularly important. However, conventional H_2 sensors are inadequate for emergent use (response time < 1 s).[28] In addition, for mobile or wearable applications, the sensor should be compatible with various substrates such as plastic, paper, and textiles.[29] Although, stretchability of the sensing element should be guaranteed, it is difficult to secure for nano-structured sensing components comprising metal or MO_x. The stretchability issue is especially critical for the flexible gas sensors using MO_x, which have excellent sensing performance for diverse gases but are mechanically brittle. This challenge can be addressed by using nanoribbon yarn structures of MO_x, which will be explained later.

First, fabricated Pd nanoribbon yarn structure was utilized for high speed H_2 gas detection. Upon exposure to H_2 gas, Pd is converted to Pd hydride and changes its resistance (**Figure 5a**). Two factors are considered in the reaction mechanism of Pd, namely, the SA:V and clamping effect. Because Pd hydride formation is initiated at the surface of Pd, a higher SA:V will result in higher sensitivity. Additionally, hydride formation includes the volume expansion of Pd. Thus, if Pd is physically bound to the substrate, the clamping effect hinders volume expansion and eventually decreases the sensitivity. For emergent use, the sensitivity and response speed of current H_2 sensors must be improved, and to this end, the clamping effect should be resolved. The suspended structure of the nanoribbon yarn of Pd can address this issue. Experiments were performed on the nanoribbon yarn and nanopattern on mold, which represent the suspended and bound states of Pd nanostructures, respectively. The results indicate that the nanoribbon yarn displays a much faster and higher response to 2% H_2 gas (τ_r = 0.8 s and $\Delta R/R_0$ = 0.309) than those for the nanopattern on mold (τ_r = 564 s and $\Delta R/R_0$ = 0.083) (Figure 5b,c). Here, τ_r refers to the "10 to 90 rise time," which is defined as the time it takes for a signal to transition from 10% to 90% of its rising waveform by the input of the target gas. Similarly, τ_f represents the "90 to 10 fall time," which denotes the time it takes for a signal to transition from 90% to 10% of its falling waveform by the removal of the target gas. The sensitivity can be improved considerably by the high SA:V

© 2024 Wiley-VCH GmbH

16136829, 2024, 38, Downloaded from https://onlinelibrary.wiley.com/doi/10.1002/smll.202311736 by Korea University Library, Wiley Online Library on [19/09/2024]. See the Terms and Conditions (https://onlinelibrary.wiley.com/terms-and-conditions) on Wiley Online Library for rules of use; OA articles are governed by the applicable Creative Commons License

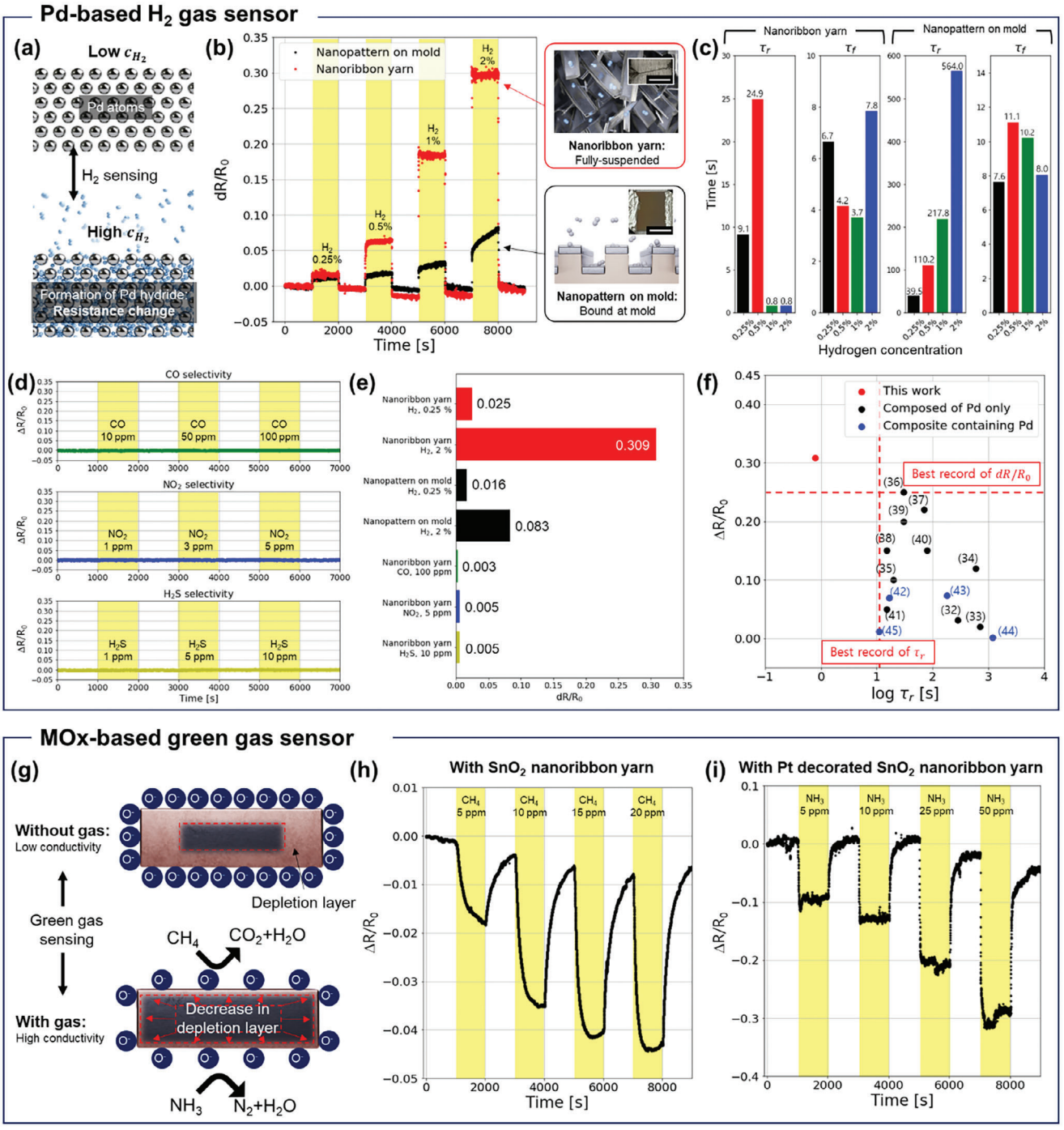


Figure 5. Applications of nanoribbon yarn as chemical sensing of green gases: a) Principle of H_2 detection by Pd; b) Comparison of the H_2 responses of the nanopattern on mold (bound) and nanoribbon yarn (suspended). The nanoribbon yarn shows higher sensitivity (3.72× @ 2% of H_2) and faster response (705× @ 2% of H_2). The inset figure depicts the schematic of each case, and the scale bar inside is 1 cm; c) Detailed comparison between the response time of the nanopattern on mold and that of nanoribbon yarn. The nanoribbon yarn displays early phase transition, indicating the elimination of the clamping effect; d,e) Selectivity test result of the nanoribbon yarn for highly reactive gases (CO, NO_2, and H_2S). The result shows that the Pd nanoribbon yarn exhibits high selectivity to H_2 only; f) Figure of merit for the proposed Pd nanoribbon yarn among currently used room-temperature-based Pd hydrogen sensors. The corresponding reference number for each point is depicted in the figure. The proposed sensor shows higher sensitivity ($\Delta R/R_0 = 0.309$) and fastest response ($\tau_r = 0.8$ s); g) Principle of detection of other green gases (CH_4 and NH_3) by SnO_2-based nanoribbon yarn; h,i) Examples of green gas sensing. Two representative green gases (CH_4 and NH_3) were monitored by SnO_2-based nanoribbon yarn without and with Pt decoration, respectively.

© 2024 Wiley-VCH GmbH

16136829, 2024, 38, Downloaded from https://onlinelibrary.wiley.com/doi/10.1002/smll.202311736 by Korea University Library, Wiley Online Library on [19/09/2024]. See the Terms and Conditions (https://onlinelibrary.wiley.com/terms-and-conditions) on Wiley Online Library for rules of use; OA articles are governed by the applicable Creative Commons License

originating from the nanoribbon itself and the suspended structure. Furthermore, the elimination of the clamping effect by the fully suspended structure of nanoribbon yarn allows for a faster and higher response.[30,31] The nanoribbon yarn displayed a faster response than that of the nanopattern on mold (705 times for 2% H_2 gas). According to previous studies, a decrease in the thickness of Pd resulted in a decrease in the response time of Pd-based H_2 sensors.[30] By suspending the structure, the effective thickness was reduced to half because H_2 molecules can approach from all sides of the nanoribbon yarn. A smaller thickness allows for faster diffusion of hydrogen into the Pd nanopattern. It should be noted that the gas should be quickly transported to individual Pd nanoribbons for a quick response. To confirm this, gas infiltration into the nanoribbon yarn was confirmed via the atomic layer deposition (ALD) of ZnO (Figure S6, Supporting Information). In addition, the decrease in response time can be attributed to the elimination of the clamping force, as reported previously.[31] The elimination of the clamping effect can be confirmed from the movement of the phase shift region. Typically, the response time of the Pd-based H_2 sensor decreases with increasing target H_2 concentration, except for the phase shift region (0.8%–2% of H_2 concentration, $\alpha \rightarrow \beta$ phase shift of Pd hydride).[30–32] In the phase shift region, this tendency is inverted, as can be observed in the initial region (0.25%–0.5%) of the nanoribbon yarn, which displayed a faster phase transition than that of the nanopattern on mold (phase transition occurred in the entire monitoring region). This result indicates that above 1% H_2 concentration, the phase shift of the nanoribbon yarn is complete, whereas that of the nanopattern on mold is not. Further, this effect enables the stable measurement of the nanoribbon yarn sensor at explosive limits, whereas the nanopattern-on-mold sensor is still unstable. Thereafter, sample-to-sample uniformity tests, specifically evaluating the rise time, fall time, and sensitivity at a representative detection target concentration of 2% H_2 gas, were performed with the five different Pd nanoribbon yarns. The rise time exhibited a value of 0.7 s with an RSD of 22.9%, the fall time recorded 8.1s with an RSD of 8.1%, and the sensitivity of 23.0% with an RSD of 21.1% (Figure S7, Supporting Information). The selectivity of the Pd nanoribbon yarn was confirmed for three different gases with high reactivities, namely, CO, NO_2, and H_2S (Figure 5d,e). For each gas, the Pd nanoribbon yarn exhibited a noise-level of response ($\Delta R/R_0$ = 0.003 for 100 ppm of CO, $\Delta R/R_0$ = 0.005 for 5 ppm of NO_2, and $\Delta R/R_0$ = 0.005 for 10 ppm of H_2S). As a result, the Pd gas sensor displayed good selectivity to H_2 gas sensing. To the best of our knowledge, this study reports the shortest response time and best sensitivity among Pd-based hydrogen sensors operating near room temperature (0–30 °C), including catalyst-decorated Pd composite sensors (Figure 5f).[32–45] Further, it reports a response time of <1 s for the first time for a room-temperature H_2 sensor.

Moreover, MOx-based gas sensors have been developed and utilized to detect other environmentally friendly gases, notably CH_4 (specifically biomethane) and NH_3. CH_4 originates from organic waste sources such as, agricultural residue, sewage, or landfill gas. Biomethane can be purified and is characterized by a reduced carbon footprint in comparison to that of conventional natural gas. Its renewable nature classifies biomethane as a green gas, which can be used for heating, electricity generation, and transportation fuel, thereby curbing greenhouse gas emissions. Similarly, NH_3 qualifies as a green gas owing to its potential as a carbon-neutral fuel and energy transporter. The sustainable Haber-Bosch process using H_2 from the renewable energy sources and N_2 from the air can generate NH_3 using renewable energy. A high energy density ensures ammonia to be suitable for energy storage and transportation, rendering it ideal for power generation, fuel cells, or as a hydrogen source for various applications.[48]

The developed MOx-based sensors for green gases measure the gas concentration by resistance change via modulation of the thickness of the depletion layer under these gases (Figure 5g). The high SA:V and fully suspended structure acquired by the nanoribbon yarn structure enable quicker and more sensitive changes in the depletion layer. A high-performance gas sensor can be accomplished via this feature. A SnO_2 nanoribbon yarn gas sensor was fabricated and used to measure the concentrations of reducing gases (CH_4[47] and NH_3[48]). It successfully detected the concentration of CH_4, with $\Delta R/R_0$ of 4.5% to 20 ppm CH_4 (Figure 5h). In addition, NH_3 gas was detected by Pt-decorated SnO_2 nanoribbon yarn with a response of ≈30% to 50 ppm NH_3 (Figure 5i).

2.4.2. Energy Transducers: TENG and Water Splitting

The proposed nanoribbon yarn can be also utilized for a green energy harvesting and as an electrochemical catalyst for the water splitting. A single-electrode TENG, in which only one side of the TENG is connected with the external load, was fabricated with nanoribbon yarn (**Figure 6a**). A mask filter comprising polypropylene and Pd nanoribbon yarn were used as the negative and positive parts in the triboelectric series, respectively (Figure 6b). The fabricated TENG can harvest the energy generated by the inhalation/exhalation motion of humans such as nose breathing, mouth breathing, coughing, and speaking (Figure 6c; Movie S1, Supporting Information). The energy was generated via TENG during the exhalation. The mouth breathing motion showed the largest peak-to-peak voltage (V_{pp} ≈ 60 V), and marked movement of the TENG elements due to the largest flow rate during the exhalation motion was observed. In addition, we confirmed that the generated energy could be stored in a capacitor (Figure 6d; Movie S2, Supporting Information). Energy harvesting and storing were successfully performed via the circuit containing the TENG, a rectifier, and a capacitor (Figure 6e) for three capacitors with different capacitances (0.1, 1, and 10 μF). Although a small difference was observed depending on the different natural discharge level of each capacitor, approximately 1.5–2 μC of charge was stored per exhalation motion. Finally, the stored energy was used to power an LED (Figure 6f; Movie S3, Supporting Information). Thus, the stored energy in the capacitor was consumed to power the LED until the voltage of the capacitor decreased to 1.5 V, the minimum driving voltage for the LED. A single exhalation released sufficient energy to power the LED.

Additionally, when Pd is applied as the constituent material of the nanoribbon yarn for the TENG, it can simultaneously be applied for H_2 sensing. Two different functions can be operated by monitoring two different parameters: V_{OC} measured for TENG operation (Figure S8a, Supporting Information) and $\Delta R/R_0$ measured for the chemoresistive H_2 sensor (Figure S8b,

© 2024 Wiley-VCH GmbH

16136829, 2024, 38, Downloaded from https://onlinelibrary.wiley.com/doi/10.1002/smll.202311736 by Korea University Library, Wiley Online Library on [19/09/2024]. See the Terms and Conditions (https://onlinelibrary.wiley.com/terms-and-conditions) on Wiley Online Library for rules of use; OA articles are governed by the applicable Creative Commons License

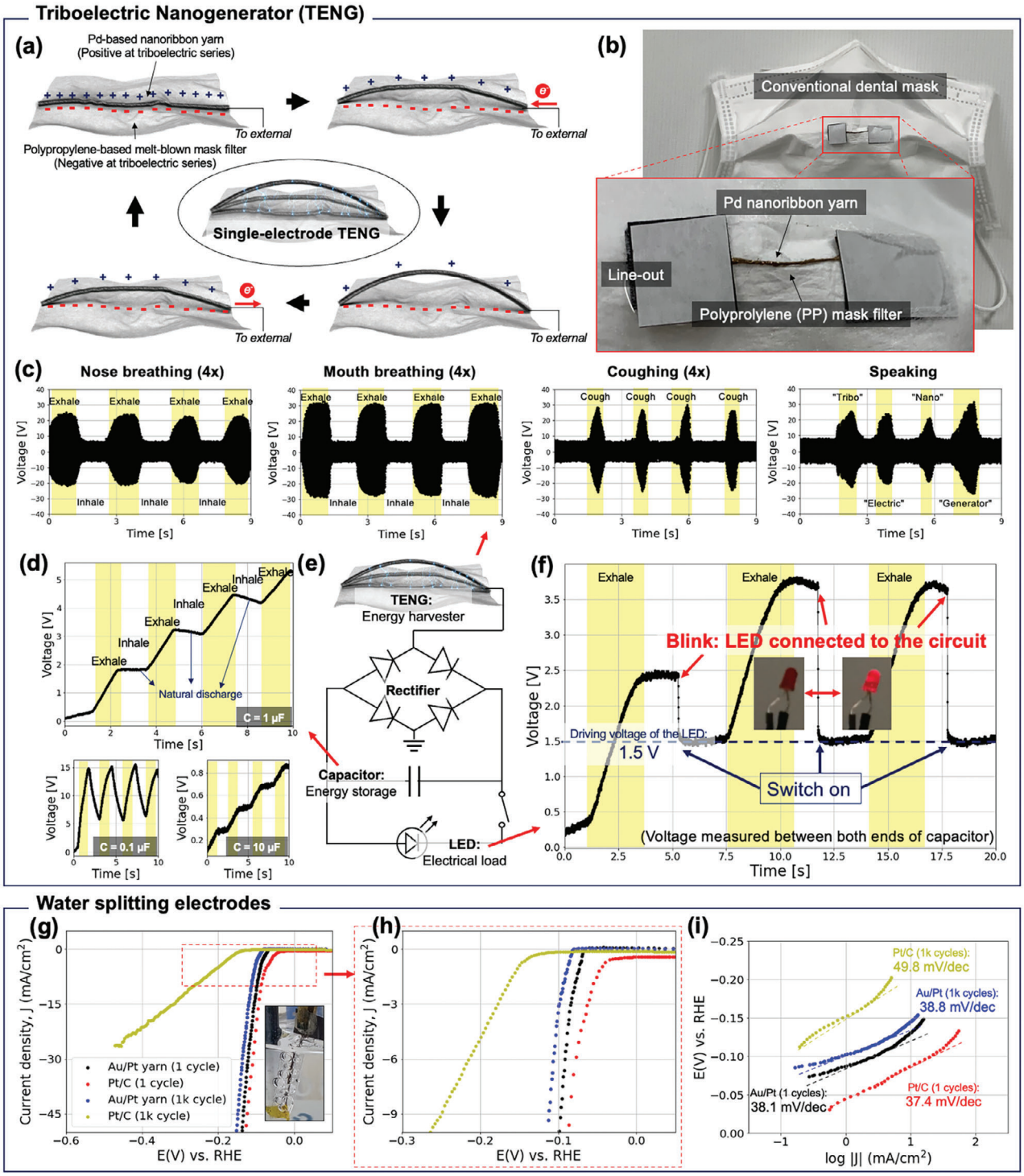


Figure 6. Applications of nanoribbon yarn as green energy transduction: a) Principle of the single-electrode TENG; b) Fabricated nanoribbon-yarn-mask–TENG. Pd nanoribbon yarn was adopted as the positive triboelectric material, and the polypropylene filter of the mask was adopted as the negative triboelectric material; c) V_{OC} generated from the proposed system for four different scenarios: nose breathing, mouth breathing, coughing, and speaking. For the speaking test, "tribo," "electric," "nano," and "generator" were spoken; d) Storing the generated energy by the proposed system in a capacitor with various capacitances (0.1, 1, and 10 μF). Approximately 1.5–2 μC of charge was stored per cycle of inhalation/exhalation; e) Schematic of the overall electrical circuits. The circuit comprised the TENG as the energy harvester, a rectifier, a capacitor for energy storage, and an LED as the electrical load; f) Result of the LED blinking test. The energy generated by the TENG was stored in the capacitor and used to power the LED; g) Electrochemical linear sweep voltammograms (LSV) of Au/Pt yarn electrode (2 cm in length) before and after 1000 cyclic voltammetry (CV) scans compared with commercial Pt/C catalyst containing 20 wt.% of Pt deposited on a glassy carbon electrode using Nafion™ as additive. (Inset) photograph of H_2 bubbling on the Au/Pt yarn electrode; h) Potential required to attain a current density of 10 mA cm^{-2} and i) corresponding Tafel plots.

© 2024 Wiley-VCH GmbH

16136829, 2024, 38, Downloaded from https://onlinelibrary.wiley.com/doi/10.1002/smll.202311736 by Korea University Library, Wiley Online Library on [19/09/2024]. See the Terms and Conditions (https://onlinelibrary.wiley.com/terms-and-conditions) on Wiley Online Library for rules of use; OA articles are governed by the applicable Creative Commons License

Supporting Information). To confirm the independence of each parameter, V_{OC} and $\Delta R/R_0$ were measured during the inhalation/exhalation motion under the same conditions. We discovered that the mask with Pd nanoribbon yarn successfully collected the triboelectric voltage (Figure S8a-i, Supporting Information), while the resistance of the Pd nanoribbon yarn remained stable (maximum $\Delta R/R_0$ of 0.0033). When a high concentration of H_2 was supplied, the Pd nanoribbon yarn displayed a marked change in resistance (Figure S8b, Supporting Information). From this series of experiments, we concluded that the Pd nanoribbon yarn attached to a mask can be independently used as both a TENG and a gas sensor, confirming that single nanoribbon yarn can be used as a multifunctional device.

Thereafter, we further implemented the Pt-decorated Au nanoribbon yarn as an electrochemical catalyst for water splitting using a standard three-electrode electrochemical configuration in 0.5 M H_2SO_4 electrolyte. Notably, the 1D form factor of yarn enables the direct application of Pt-decorated Au nanoribbon yarn as an electrode without the requirement of any additives unlike the commercial Pt/C catalyst. Typically, Pt/C catalyst ink is prepared with Nafion, as a binding agent, which is then coated on a conductive electrode support such as a glassy carbon electrode.[49] However, the Pt/C catalyst experiences a loss of active catalyst due to the dissolution of Nafion during extended electrochemical cycling and the agglomeration of Pt particles through diffusion on the carbon support, resulting in a decrease in its electrochemical activity.[50,51] This reduction in activity is clearly illustrated in Figure 6g, in which the Pt/C catalyst exhibits a marked decrease in activity for the hydrogen evolution reaction (HER) after 1000 cycles. By contrast, the Pt-decorated Au nanoribbon yarn electrode demonstrates a comparable over-potential (97.5 mV) with that of the commercial Pt/C catalyst (85 mV versus reversible hydrogen electrode (RHE) reference) in the first cycle at a current density (j) of 10 mA cm^{-2} (Figure 6h). After 1000 cycles, the Pt/C electrode exhibited a marked loss of activity as evidenced by an increased over-potential of 264.6 mV. The Pt-decorated Au nanoribbon yarn electrode, however, displayed superior durability, maintaining a comparable over-potential (111.2 mV at j of 10 mA cm^{-2}) to that of its initial activity (Figure 6i). To investigate the hydrogen evolution mechanism, we analyzed the linear portion of the Tafel plot ($\eta = b \log j + a$, where η is the over-potential, b is the Tafel slope, and j is the current density). A change in the Tafel slope with increasing potential can be attributed to a change in either the reaction mechanism or pathway due to changes in the surface coverage of intermediates.[52,53] The Pt/C reference sample, exhibits the smallest Tafel slope (37.4 mV dec^{-1}). The Pt-decorated Au nanoribbon yarn electrode displayed a comparable Tafel slope of 38.1 mV dec^{-1} to that of Pt/C indicating similarity in the reaction mechanism. Remarkably, the Pt-decorated Au nanoribbon yarn electrode maintained its Tafel slope (38.8 mV dec^{-1}), whereas the precious metal catalyst Pt/C displayed much higher slope (49.8 mV dec^{-1}) after 1000 cycles. The stability and the application feasibility due to the yarn structure enabling the direct usage of Pt-decorated Au nanoribbon yarn as the electrode without the requirement of any additives, demonstrate the relevance of our yarn for cost effective and highly durable energy production.

3. Conclusion

A facile fabrication method of the nanoribbon yarn with inorganic materials was proposed in this research. The nanoribbon yarn was fabricated as follows: deposition of the target inorganic material on the replicated nanoimprinted mold, plasma etching of the mold, and twisting of released nanostructures into a yarn configuration. Nanoyarns with a variety of materials (Au, Pd, Ni, Al, Pt, WO_3, SnO_2, NiO, In_2O_3, and CuO) were accomplished by the PVD process. The fabricated nanoribbon yarn showed good stretchability of the yarn structure and high SA:V of the fully-suspended nanostructure. These features are useful in green energy applications such as metal and MOx-based green gas sensors (Pd nanoribbon yarn as a H_2 gas sensor, SnO_2-based nanoribbon yarn as a CH_4 gas sensor, and Pt-decorated SnO_2-based nanoribbon yarn as an NH_3 gas sensor), a TENG (between Pd nanoribbon yarn and PPy-based mask filter), and a electrochemical electrode for water splitting (Pt-decorated Au nanoribbon yarn).

Because the inorganic nanoribbon yarn successfully confers the advantages of nanostructures (e.g., high SA:V, high flexibility) to the macrostructure yarn, it can be widely adopted in various applications. For example, the advantages of nanoribbon yarn can be synergistically adopted in other flexible energy-related devices, such as fiber supercapacitors and flexible thermoelectric generators. We believe that the proposed method can provide the breakthrough that necessitates the use of flexible inorganic materials.

4. Experimental Section

Fabrication of the Nanoribbon Yarn: Replication of the nanoline mold was conducted using a master Si nanoline mold (width (w): 800 nm, pitch (p): 2000 nm, depth (h): 1200 nm, (w, p, h) = (200, 400, 400) [nm] of mold was used for various morphology tests) that was fabricated by the KrF lithography and deep reactive ion etching (DRIE) processes. The replica was nanoimprinted by UV-curable PUA resin (RM-311, Minuta Technology Co., Ltd., Korea) with polyethylene terephthalate (PET) substrate (t = 0.1 mm) (Figure S1a-i, ii, Supporting Information).[33,54–56] The target material was deposited onto the replicated nanoline mold via electron beam evaporation (deposition rate of 5 Å s^{-1}, Daeki Hi-Tech Co., Ltd., Korea) (Figure S1a-iii, Supporting Information). Details of the deposition thickness of each material are listed in Table S1 (Supporting Information). Next, the target material deposited onto the nanoline molds with dimensions of 2 × 2 cm^2 for the material versatility test and 12 × 2 cm^2 for the large-area demonstration were etched by RIE (Sorona, Korea) with a power of 50 W, etch gases O_2 (100 sccm) and CF_4 (20 sccm), a working pressure of 200 mTorr, and an etch time of 10 min (Figure S1b-i, ii, Supporting Information). After 10 min (4 min for various morphology tests) of etching, the PUA nanoline mold was sufficiently undercut, and the material deposited onto that mold was suspended as shown in Figure S2 (Supporting Information).[57,58] The single end of the suspended nanoline-patterned materials was attached with Kapton tape and delaminated from the mold (Figure S1c-i, Supporting Information). After delamination, the other end was fixed by a tweezer and twisted to form a nanoribbon yarn (Figure S1c-ii,iii, Supporting Information).

Strain and Bend Test: For the strain test, the nanoribbon yarn (100 nm of Au was deposited) with a length of ≈2 cm was prepared and attached to a custom-made linear stage with a carbon tape. A coating of silver paste was applied for interconnection to the external electrical wires. Strain was applied at a strain rate of 0.01 s^{-1} (custom-built strain test setup), and the resistance of the nanoribbon yarn was monitored during the strain test (2400 SMU, Keithley, USA). For the bend test, the nanoribbon yarn was

© 2024 Wiley-VCH GmbH

16136829, 2024, 38, Downloaded from https://onlinelibrary.wiley.com/doi/10.1002/smll.202311736 by Korea University Library, Wiley Online Library on [19/09/2024]. See the Terms and Conditions (https://onlinelibrary.wiley.com/terms-and-conditions) on Wiley Online Library for rules of use; OA articles are governed by the applicable Creative Commons License

fixed onto the PET film (t = 0.1 mm) using the same experimental setup (custom-built strain test setup and 2400 SMU) by applying silver paste at both ends of the nanoribbon yarn, and an external electrical wire was connected. The specimen was attached onto the linear stage and buckled by compression. A gap decrement of 0.18 cm per step was performed with an initial gap of 5.55 cm, and the curvature and resistance of the nanoribbon yarn were measured per step. Twenty-six decrements from 5.55 to 0.87 cm were performed, and the resulting curvature changed from 0 to 2.32 cm^{-1}.

Gas Sensing Test: Gas sensing tests for H_2, NH_3, and CH_4 gases were performed using Pd-, SnO_2-, and Pt-decorated SnO_2 nanoribbon-yarn-based gas sensors, respectively, under atmospheric pressure in a gas chamber setup. A schematic of the gas chamber setup is shown in Figure S9a (Supporting Information). The concentration of each gas injected into the gas chamber was controlled by mass flow controllers (AFC500, ATOVAC, Korea), and the total gas flow rate was set to 500 sccm. The NH_3 and CH_4 gas tests were performed at 250 °C in a tube furnace for activation of the gas reaction between the target gases and nanoribbon yarn. The H_2 gas test was performed at ambient temperature of 25 °C. In the gas tests, the current passing through the nanoribbon yarn was measured by a source meter (2400 SMU, Keithley, USA), with an input voltage of 3 V. The response and recovery times were evaluated for the response of $\Delta R/R_0$ = 10%–90% and 90%–10%, respectively. For the gas selectivity test, the concentration of each tested gas was set close to the permissible exposure or lower explosive limit according to the safety guidelines (toxic and hazardous substances 1915.1000) defined by the occupational safety and health administration (OSHA).[59]

ALD Coating for Confirmation of the Gas Infiltration: Zinc oxide was decorated onto the Pd nanoyarn surface via ALD using a homemade ALD reactor (ICOT mini, ICOT). Diethylzinc, deionized water, and nitrogen gas were used as the precursor, oxidant, and carrier gas, respectively. The temperature of the reactor chamber was maintained at 155 °C during operation. After 0.5 s of precursor/oxidant pulse, 10 sccm of carrier gas flow was applied for 90 s. Thereafter, the operation chamber was vacuumed for 90 s to lower the chamber pressure to <30 mTorr and to facilitate the penetration of the precursor into the complex 3D structure of the nanoribbon yarn. After 200 cycles of ALD, the thickness of deposited zinc oxide was ≈40 nm.

TENG Test: The single-electrode TENG was prepared by integrating Pd nanoribbon yarn directly onto the polypropylene (PP)-based melt-blown mask filter (mask–TENG system). The nanoribbon yarn was attached with carbon tape, and the external electrical wire was connected to the carbon tape. Three tests were performed with this setup, namely, the TENG, capacitor charging, and LED blinking tests. For the TENG test, four scenarios (nose breathing, mouth breathing, coughing, and speaking) were tested. The V_{OC} between the ground and electrical wire from the mask–TENG system was measured using an oscilloscope (MDO3022, Tektronics, USA). For the capacitor charging test, three tests for three different capacitors (capacitances of 0.1, 1, and 10 μF) were performed. Each end of the capacitor circuits (Figure 5e) with opened switches was connected to the oscilloscope, and the voltage was measured during repeated exhalation and inhalation cycles. For the LED blinking test, the capacitor with a capacitance of 1 μF with a single exhalation was used; the opened switch was first charged and thereafter switched off to power the LED by the electrical energy generated.

Details of the Multifunctional Usage of Nanoribbon Yarn: Three tests were performed to confirm the multifunctional usage of nanoribbon yarn: breathing test with V_{OC} measurement, breathing test with resistance measurement, and H_2 sensing test with resistance measurement. The V_{OC} was measured using an oscilloscope (MDO3022, Tektronics, USA) and the resistance was measured by a source meter (2400 SMU, Keithley, USA). For the breathing test, the mask–TENG system was worn, and the repeated exhalation/inhalation test was performed. For the H_2 sensing test, in an open environment, a gas with a 2% hydrogen concentration was injected from a tube nearby the mask (Figure S9b, Supporting Information).

Water Splitting Test: Electrochemical measurements were performed using a Bio-Logic SP-200 potentiostat and a three-electrode electrochemical cell setup. The Pt-decorated Au nanoribbon yarn served as the working electrode, while a Pt wire acted as the counter electrode, and a saturated calomel electrode (SCE) was used as the reference electrode. The commercial Pt/C (Sigma Aldrich) containing 20 wt.% Pt was used for comparison. To prepare the Pt/C catalyst, an equivalent Pt weight (0.06 mg) to that of the Pt-decorated Au nanoribbon yarn was dispersed in ethanol and directly deposited onto the working electrode using a micropipette. The electrode was thereafter dried at 60 °C under a flow of nitrogen gas. A protective layer of 10 μL of 5% Nafion was deposited on the sample surface placed on a glassy carbon electrode. Pt contamination was ruled out by repeating the same experiments with a carbon counter electrode. The reference electrode was calibrated to the reversible hydrogen electrode (RHE) potential in a 0.5 M H_2SO_4 electrolyte, using a Pt wire as both the counter and working electrode. The calibration yielded ERHE = ESCE + 0.254 V. Throughout the electrochemical tests, the electrolyte was continuously stirred using a magnetic stirrer to facilitate mass transport and prevent the accumulation of bubbles on the electrode surface. The HER activity was evaluated using LSV in the voltage range of 0.1 to −0.5 V versus RHE, with a scan rate of 5 mV s^{-1}. Prior to the LSV measurement, a CV test consisting of 10 cycles was performed at a scan rate of 50 mV s^{-1} to activate the working electrode. To assess stability, a CV scan was repeated for more than 1000 cycles at a rate of 100 mV s^{-1}.

Supporting Information

Supporting Information is available from the Wiley Online Library or from the author.

Acknowledgements

J.A., Y.J., and M.K. contributed equally to this work. **Funding statement**: This research was supported by the Basic Research Program of KIMM (Korea Institute of Machinery and Materials, NK248B) and the Development Program of Machinery and Equipment Industrial Technology (20 018 235, Development of inline nano-imprinter for nano photonic device) funded by the Ministry of Trade, industry & Energy (MI, Korea). This research was supported by the National Research Foundation of Korea (NRF) grant funded by the Korea government (MSIT). (No. 2021R1A2C300874212) This work was supported by Multi-Ministry Collaborative R&D Program (Development of Techniques for Identification and Analysis of Gas Molecules to Protect Against Toxic Substances) through the National Research Foundation of Korea (NRF) funded by KNPA, MSIT, MOTIE, ME, NFA (NRF-2017M3D9A1073858). This results was also supported by "Rigional Innovation Strategy (RIS)" through the National Research Foundation of Korea(NRF) funded by the Ministry of Education(MOE)(2021RIS-004).

Conflict of Interest

The authors declare no conflict of interest.

Data Availability Statement

The data that support the findings of this study are available from the corresponding author upon reasonable request.

Keywords

gas sensor, inorganic material, nanoribbon yarn, triboelectric nanogenerator, water splitting

Received: December 16, 2023
Revised: March 15, 2024
Published online: March 29, 2024

© 2024 Wiley-VCH GmbH

16136829, 2024, 38, Downloaded from https://onlinelibrary.wiley.com/doi/10.1002/smll.202311736 by Korea University Library, Wiley Online Library on [19/09/2024]. See the Terms and Conditions (https://onlinelibrary.wiley.com/terms-and-conditions) on Wiley Online Library for rules of use; OA articles are governed by the applicable Creative Commons License

[1] Y. Lim, Y. Lee, J. il Heo, H. Shin, *Sens Actuators B Chem* **2015**, *210*, 218.
[2] J. S. Lee, K. W. Choi, J. Y. Yoo, M. S. Jo, J. B. Yoon, *Small* **2020**, *16*, 1906845.
[3] A. I. Fedorchenko, A. B. Wang, H. H. Cheng, *Appl. Phys. Lett.* **2009**, *94*, 152111.
[4] F. H. Gojny, M. H. G. Wichmann, B. Fiedler, W. Bauhofer, K. Schulte, *Compos Part A Appl Sci Manuf* **2005**, *36*, 1525.
[5] Y. J. Yun, W. G. Hong, N. J. Choi, B. H. Kim, Y. Jun, H. K. Lee, *Sci. Rep.* **2015**, *5*, 10904.
[6] J. Choi, Y. Jung, S. J. Yang, J. Y. Oh, J. Oh, K. Jo, J. G. Son, S. E. Moon, C. R. Park, H. Kim, *ACS Nano* **2017**, *11*, 7608.
[7] K. T. Park, Y. S. Cho, I. Jeong, D. Jang, H. Cho, Y. Choi, T. Lee, Y. Ko, J. Choi, S. Y. Hong, M. W. Oh, S. Chung, C. R. Park, H. Kim, *Adv. Energy Mater.* **2022**, *12*, 2200256.
[8] X. He, Y. Zi, H. Guo, H. Zheng, Y. Xi, C. Wu, J. Wang, W. Zhang, C. Lu, Z. L. Wang, *Adv. Funct. Mater.* **2017**, *27*, 1604378.
[9] K. Dong, X. Peng, Z. L. Wang, *Adv. Mater.* **2020**, *32*, 1902549.
[10] J. Wang, X. Li, Y. Zi, S. Wang, Z. Li, L. Zheng, F. Yi, S. Li, Z. L. Wang, *Adv. Mater.* **2015**, *27*, 4830.
[11] V. T. Le, H. Kim, A. Ghosh, J. Kim, J. Chang, Q. A. Vu, D. T. Pham, J. H. Lee, S. W. Kim, Y. H. Lee, *ACS Nano* **2013**, *7*, 5940.
[12] G. Qu, J. Cheng, X. Li, D. Yuan, P. Chen, X. Chen, B. Wang, H. Peng, *Adv. Mater.* **2016**, *28*, 3646.
[13] W. Son, D. W. Lee, Y. K. Kim, S. Chun, J. M. Lee, J. H. Choi, W. S. Shim, D. Suh, S. K. Lim, C. Choi, *ACS Sens.* **2023**, *8*, 94.
[14] K. Jiang, Q. Li, S. Fan, *Nature* **2002**, *419*, 801.
[15] X. H. Zhong, Y. L. Li, Y. K. Liu, X. H. Qiao, Y. Feng, J. Liang, J. Jin, L. Zhu, F. Hou, J. Y. Li, *Adv. Mater.* **2010**, *22*, 692.
[16] S. H. Aboutalebi, R. Jalili, D. Esrafilzadeh, M. Salari, Z. Gholamvand, S. Aminorroaya Yamini, K. Konstantinov, R. L. Shepherd, J. Chen, S. E. Moulton, P. C. Innis, A. I. Minett, J. M. Razal, G. G. Wallace, *ACS Nano* **2014**, *8*, 2456.
[17] J. Carretero-González, E. Castillo-Martínez, M. Dias-Lima, M. Acik, D. M. Rogers, J. Sovich, C. S. Haines, X. Leprõ, M. Kozlov, A. Zhakidov, Y. Chabal, R. H. Baughman, *Adv. Mater.* **2012**, *24*, 5695.
[18] A. S. Levitt, C. E. Knittel, R. Vallett, M. Koerner, G. Dion, C. L. Schauer, *J. Appl. Polym. Sci.* **2017**, *134*, app44813.
[19] S. Wu, B. Duan, P. Liu, C. Zhang, X. Qin, J. T. Butcher, *ACS Appl. Mater. Interfaces* **2016**, *8*, 16950.
[20] Z. Dai, F. Yan, M. Qin, X. Yan, *e-Polymers* **2020**, *20*, 600.
[21] L. Li, K. Wang, H. Fan, X. Zhu, J. Mu, H. Yu, Q. Zhang, Y. Li, C. Hou, H. Wang, *Mater. Horiz.* **2021**, *8*, 1711.
[22] S. H. Kim, C. S. Haines, N. Li, K. J. Kim, T. J. Mun, C. Choi, J. Di, Y. J. Oh, J. P. Oviedo, J. Bykova, S. Fang, N. Jiang, Z. Liu, R. Wang, P. Kumar, R. Qiao, S. Priya, K. Cho, M. Kim, M. S. Lucas, L. F. Drummy, B. Maruyama, D. Y. Lee, X. Lepró, E. Gao, D. Albarq, R. Ovalle-Robles, S. J. Kim, †. Ray, H. Baughman, *Science* **2017**, *357*, 773.
[23] Q. Jin, S. Jiang, Y. Zhao, D. Wang, J. Qiu, D. M. Tang, J. Tan, D. M. Sun, P. X. Hou, X. Q. Chen, K. Tai, N. Gao, C. Liu, H. M. Cheng, X. Jiang, *Nat. Mater.* **2019**, *18*, 62.
[24] X. Chen, C. Li, M. Grätzel, R. Kostecki, S. S. Mao, *Chem. Soc. Rev.* **2012**, *41*, 7909.
[25] M. Amjadi, A. Pichitpajongkit, S. Lee, S. Ryu, I. Park, *ACS Nano* **2014**, *8*, 5154.
[26] J. Gu, D. Kwon, J. Ahn, I. Park, *ACS Appl. Mater. Interfaces* **2020**, *12*, 10908.
[27] Hydrogen Council and McKinsey & Company, Hydrogen for Net-Zero, https://hydrogencouncil.com/wp-content/uploads/2021/11/Hydrogen-for-Net-Zero.pdf, (accessed: September 2023).
[28] T. Hübert, L. Boon-Brett, G. Black, U. Banach, *Sens Actuators B Chem* **2011**, *157*, 329.
[29] R. Alrammouz, J. Podlecki, P. Abboud, B. Sorli, R. Habchi, *Sens Actuators A Phys* **2018**, *284*, 209.
[30] F. Yang, D. K. Taggart, R. M. Penner, *Nano Lett.* **2009**, *9*, 2177.
[31] B. Wang, L. Sun, M. Schneider-Ramelow, K. D. Lang, H. D. Ngo, *Micromachines (Basel)* **2021**, *12*, 1429.
[32] Z. J. Zhao, J. Ahn, D. Lee, C. B. Jeong, M. Kang, J. Choi, M. Bok, S. Hwang, S. Jeon, S. Park, J. Ko, K. S. Chang, J. W. Choi, I. Park, J. H. Jeong, *Nanoscale* **2022**, *14*, 1136.
[33] J. Ko, Z. J. Zhao, S. H. Hwang, H. J. Kang, J. Ahn, S. Jeon, M. Bok, Y. Jeong, K. Kang, I. Cho, J. H. Jeong, I. Park, *ACS Nano* **2020**, *14*, 2191.
[34] H. J. Noh, H. J. Kim, Y. M. Park, J. S. Park, H. N. Lee, *Appl. Surf. Sci.* **2019**, *480*, 52.
[35] X. Q. Zeng, M. L. Latimer, Z. L. Xiao, S. Panuganti, U. Welp, W. K. Kwok, T. Xu, *Nano Lett.* **2011**, *11*, 262.
[36] D. H. Baek, J. Choi, J. Kim, *Sens Actuators B Chem* **2019**, *284*, 362.
[37] M. S. Jo, K. H. Kim, K. W. Choi, J. S. Lee, J. Y. Yoo, S. H. Kim, H. Jin, M. H. Seo, J. B. Yoon, *ACS Nano* **2022**, *16*, 11957.
[38] F. Yang, D. K. Taggart, R. M. Penner, *Nano Lett.* **2009**, *9*, 2177.
[39] F. Yang, S. C. Kung, M. Cheng, J. C. Hemminger, R. M. Penner, *ACS Nano* **2010**, *4*, 5233.
[40] K. J. Jeon, J. M. Lee, E. Lee, W. Lee, *Nanotechnology* **2009**, *20*, 135502.
[41] P. Offermans, H. D. Tong, C. J. M. van Rijn, P. Merken, S. H. Brongersma, M. Crego-Calama, *Appl. Phys. Lett.* **2009**, *94*, 223110.
[42] Z. J. Zhao, J. Ko, J. Ahn, M. Bok, M. Gao, S. H. Hwang, H. J. Kang, S. Jeon, I. Park, J. H. Jeong, I. Park, J. H. Jeong, *ACS Sens.* **2020**, *5*, 2367.
[43] X. Tang, P. A. Haddad, N. Mager, X. Geng, N. Reckinger, S. Hermans, M. Debliquy, J. P. Raskin, *Sci. Rep.* **2019**, *9*, 3653.
[44] K. Yu, X. Tian, X. Wang, F. Yang, T. Qi, J. Zuo, *Sens Actuators B Chem* **2019**, *299*, 126989.
[45] M. Cho, J. Zhu, H. Kim, K. Kang, I. Park, *ACS Appl. Mater. Interfaces* **2019**, *11*, 13343.
[46] O. Grasham, V. Dupont, T. Cockerill, M. A. Camargo-Valero, M. V. Twigg, *Sustain Energy Fuels* **2020**, *4*, 5835.
[47] S. Navazani, A. Shokuhfar, M. Hassanisadi, M. Askarieh, A. di Carlo, A. Agresti, *Talanta* **2018**, *181*, 422.
[48] N. van Hieu, L. T. B. Thuy, N. D. Chien, *Sens Actuators B Chem* **2008**, *129*, 888.
[49] S. Padmajan Sasikala, Y. Singh, L. Bing, T. Yun, S. H. Koo, Y. Jung, S. O. Kim, *Nat. Commun.* **2020**, *11*, 5032.
[50] H. Yuan, H. Song, X. Qiu, W. Zhu, L. Chen, *Electrochem. Commun.* **2010**, *12*, 14.
[51] S. Padmajan Sasikala, S. H. Kim, C. Park, D. H. Kim, H. J. Jung, J. Jung, H. Lee, P. Li, H. Kim, S. Hong, S. Y. Choi, I. D. Kim, P. Prabhakaran, K. S. Lee, S. O. Kim, *Mater. Today* **2022**, *58*, 18.
[52] K. E. Lee, S. P. Sasikala, H. J. Lee, G. Y. Lee, S. H. Koo, T. Yun, H. J. Jung, I. H. Kim, S. O. Kim, *Particle and Particle Systems Characterization* **2017**, *34*, 1600375.
[53] A. Alobaid, C. Wang, R. A. Adomaitis, *J. Electrochem. Soc.* **2018**, *165*, J3395.
[54] S. H. Hwang, Z. J. Zhao, S. Jeon, H. Kang, J. Ahn, J. H. Jeong, *Nanoscale* **2019**, *11*, 11128.
[55] Y. Jeong, H. jung Kang, Z. jun Zhao, J. Ahn, S. Hyoung Hwang, S. Jeon, J. Ko, J. Y. Jung, I. Park, J. ho Jeong, *Appl. Surf. Sci.* **2021**, *552*, 149500.
[56] Z. J. Zhao, J. Ahn, D. Lee, C. B. Jeong, M. Kang, J. Choi, M. Bok, S. Hwang, S. Jeon, S. Park, J. Ko, K. S. Chang, J. W. Choi, I. Park, J. H. Jeong, *Nanoscale* **2022**, *14*, 1136.
[57] J. Ahn, J. Gu, Y. Jeong, J. H. Ha, J. Ko, B. Kang, S. H. Hwang, J. Park, S. Jeon, H. Kim, J. H. Jeong, I. Park, *ACS Nano* **2023**, *17*, 5935.
[58] J. Ahn, J. H. Ha, Y. Jeong, Y. Jung, J. Choi, J. Gu, S. H. Hwang, M. Kang, J. Ko, S. Cho, H. Han, K. Kang, J. Park, S. Jeon, J. H. Jeong, I. Park, *Nat. Commun.* **2023**, *14*, 833.
[59] Occupational Safety and Health Administration (OSHA), Toxic and hazardous substances, Occupational Safety and Health Administration DC **2017**, p. 1915.1000.

© 2024 Wiley-VCH GmbH

16136829, 2024, 38, Downloaded from https://onlinelibrary.wiley.com/doi/10.1002/smll.202311736 by Korea University Library, Wiley Online Library on [19/09/2024]. See the Terms and Conditions (https://onlinelibrary.wiley.com/terms-and-conditions) on Wiley Online Library for rules of use; OA articles are governed by the applicable Creative Commons License